BOLETIN DE LA SOCIEDAD ESPAÑOLA DE
Cerámica y Vidrio
www.elsevier.es/bsecv

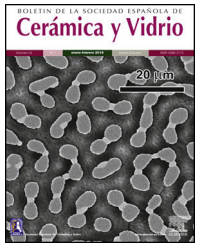

Synthesis and characterization of semi-transparent gehlenite ceramic spheres obtained by selective laser sintering

Linda Viviana García-Quiñonez[a], *Adolfo López-Liévano*[b], *Adolfo Collado-Hernández*[c], *Nora Elizondo-Villarreal*[c], *Eden Amaral Rodríguez-Castellanos*[d], *Guadalupe Alan Castillo-Rodríguez*[d], *Nayely Pineda-Aguilar*[e], *José Eduardo Terrazas-Rodríguez*[f], *Daniel Fernández-González*[g], *Cristian Gómez-Rodríguez*[b,*]

[a] *Centro de Investigación en Recursos Energéticos y Sustentables (CIRES), Universidad Veracruzana, Av. Universidad Veracruzana km 7.5, Col. Santa Isabel I, 96538 Coatzacoalcos, Veracruz, Mexico*
[b] *Facultad de Ingeniería, Campus Coatzacoalcos, Universidad Veracruzana, Av. Universidad km 7.5, Col. Santa Isabel, 96535 Coatzacoalcos, Veracruz, Mexico*
[c] *Physical Mathematical Scientific Research Center (CICFIM), Universidad Autónoma de Nuevo León, Cd. Universitaria, 66455 San Nicolás de los Garza, Nuevo León, Mexico*
[d] *Facultad de Ingeniería Mecánica y Eléctrica (FIME), Universidad Autónoma de Nuevo León, Ave. Pedro de Alba s/n, Cd. Universitaria, 66451 San Nicolás de los Garza, Nuevo León, Mexico*
[e] *Centro de Investigación en Materiales Avanzados, S.C. (CIMAV), Unidad Monterrey, Alianza Norte 202, Parque de Investigación e Innovación Tecnológica, 66628 Apodaca, Nuevo León, Mexico*
[f] *Facultad de Ciencias Químicas, Universidad Veracruzana, Campus Coatzacoalcos, Av. Universidad km 7.5, Col. Santa Isabel, 96538 Coatzacoalcos, Veracruz, Mexico*
[g] *Nanomaterials and Nanotechnology Research Center (CINN-CSIC), Universidad de Oviedo (UO), Principado de Asturias (PA), Avda. de la Vega, 4-6, 33940 El Entrego, Asturias, Spain*

ARTICLE INFO

Article history:
Received 29 May 2024
Accepted 16 September 2024
Available online 25 September 2024

Keywords:
Selective laser sintering
Ceramic oxides
Ceramics spheres

ABSTRACT

Selective laser sintering (SLS) is a novel additive manufacturing technique that has been recently applied to the sintering of powdered materials. In this work, radiation with laser was applied to a ceramic oxide powder blend to develop semi-transparent ceramic spheres. The powders bed consisted of different ceramics oxides which were irradiated with a continuous CO_2 laser ($\lambda = 10.6\ \mu m$) with a power density of 155 W/cm^2, at both; static (punctually radiated) and non-static (dynamic) conditions. X-ray diffraction confirmed the presence of silicate phases, "gehlenite type". Punctually radiated samples show semi-spheres with a completely sintered surface without visible cracks, however there were aggregates that did not fuse in the matrix. On the contrary, the use of dynamic radiation decreased the number

* *Corresponding author.*
E-mail address: crisgomez@uv.mx (C. Gómez-Rodríguez).
https://doi.org/10.1016/j.bsecv.2024.09.004

of aggregates in the ceramic spheres, and a homogeneous sintered surface was obtained. Raman spectra show the introduction of the ceramic oxides into the silica matrix when the powder blend is punctually radiated with laser, while the dynamic parameters aid the crystallization of the silica matrix. Therefore, laser sintering using a continuous laser source with non-static radiation is a better alternative to produce semi-transparent ceramic spheres from a ceramic oxide powder bed with greater densification and better optical properties in transmittance–reflectance.

Síntesis y caracterización de esferas de gehlenita semitransparente obtenidas por sinterización selectiva de láser

Palabras clave:
Sinterización selectiva por láser
Óxidos cerámicos
Esferas cerámicas

RESUMEN

La sinterización selectiva por láser (SSL) es una novedosa técnica de fabricación aditiva que se ha aplicado en sinterización de materiales. En este trabajo se aplicó una radiación láser a una mezcla de polvos de óxido cerámico para desarrollar esferas semitransparentes. El lecho de polvos estuvo formado por diferentes óxidos cerámicos, los cuales fueron radiados con un láser continuo de CO_2 ($\lambda = 10.6\,\mu m$) con densidad de potencia de $155\,W/cm^2$, tanto en condiciones de radiación puntual y dinámica. La difracción de rayos X confirmó la presencia de fases de silicato «tipo gehlenita». Las muestras puntualmente radiadas con láser mostraron semiesferas con una superficie completamente sinterizada sin grietas, con agregados que no fusionaron en la matriz. El uso de una radiación dinámica disminuyó el número de agregados en las esferas cerámicas con una superficie sinterizada homogénea. Así mismo, la espectroscopía Raman mostró la introducción de los óxidos cerámicos en la matriz de sílice cuando los polvos fueron radiados puntualmente con el láser, mientras que la radiación dinámica ayudó a la cristalización de la matriz de sílice. Por lo tanto, la sinterización láser que utiliza una radiación dinámica es una mejor alternativa para producir esferas cerámicas semitransparentes desde polvos de óxidos cerámicos obteniendo densificación y mejores propiedades ópticas en transmitancia-reflectancia.

Introduction

Selective laser sintering (SLS) is a prototyping process capable of manufacturing fully functional parts of objects, mainly with small complex forms, high precision workpiece contours and specific surface finishes, which are hardly obtained by other processes [1,2]. This method has been recently employed due to its suitability to process almost any material: metals, polymers and ceramics, using short processing times during sintering and conforming of materials, and it can be implemented at ambient pressure and room temperature [1,2]. In SLS, generally, a CO_2 or Nd:YAG laser are used to form a complete component from powdered materials, where in some cases intermediate binders are used [3,4]. In both types of lasers, parameters such as power, scanning speed, and exposure time, play an important role during the sintering of a material. Laser power controls the energy available for the process, while scanning speed doses the transfer of energy to the powder bed by unit area; together, regulate the length, width and thickness of the irradiated zone [5].

In some materials, such as ceramics make SLS a challenging, since when the pieces are heated up in some case to melting point, and subsequent cooling, formation of cracks can be produced due to the difference in thermal expansion coefficients of the in situ generated phases, and low or no plasticity [6], due to this the energy used to bond ceramic powders must be controlled to achieve a sintered piece with good thermal, mechanical, chemical, and physical properties.

Furthermore, sintering of pieces containing refractory oxide powders is achieved, in general, by solid-state diffusion, if there is no binding phase; besides, sufficient exposure time is required to achieve desired densities [7].

In SLS, the required laser energy in each sample is based primarily on: (a) the composition of the mixed powder (characteristics and properties) and (b) the wavelength at which each material can absorb radiation, i.e. optical properties play an important role, and this parameter can be analyzed with the penetration depth of the incident light and is determined by the transmittance and absorbance of the powder blend [8,9]. When SLS is implemented to produce parts from powders of the same type, the process is called direct sintering and when mixtures of different powders are processed, it is known as indirect sintering. In the latter case, one of the powders acts as a wetting phase and helps to bind the grains with a higher melting point, obtaining densified pieces. The

use of additives as binders, organic or inorganic, aids the sintering process to achieve also densified pieces and the desired properties. In the context of transparent ceramics, the use of additives could compromise the transparency of the material due to the increment of pores upon decomposition of the additives, especially organic compounds such as resins, plasticizers, and dispersants [10]. In this sense, transparent ceramics are polycrystalline refractory materials with some light transmittance, which emerged as candidates to replace single crystals; these materials are used in different applications, such as transparent sapphire or Al_2O_3 armors resistant against projectiles, laser hosts, electromagnetic windows, smartphone screens, biomedical materials, among others. Furthermore, these materials are characterized by their high thermal resistance, high hardness, resistance to corrosion, optical transparency, and can be used under extreme conditions. Transparent ceramics have been obtained by different techniques, such as: high-pressure (HP) sintering, high isostatic pressure (HIP) sintering [11], via aqueous gel-casting and vacuum sintering [12], microwave sintering [13], conventional sintering [14], spark plasma sintering [15,16], solid-state reaction and flame synthesis [17]. With these techniques, transparent ceramics with different compositions have been studied, including simple oxides, sesquioxides, complex oxides and aluminum oxynitride, such as Al_2O_3 [18], ZrO_2 [19], Y_2O_3 [20], Lu_2O_3 [21], MgO, $Y_3Al_5O_{12}$, $MgAl_2O_4$, aluminum oxynitride, among others.

General processing of transparent ceramics consists of synthesis of precursor powder, compacting, calcination/sintering and post-treatment (annealing, machining and polishing). There have been recent works related to the manufacturing of ceramic transparent ceramics, such as, Yamazaki et al. where they studied a transparent Cr^{4+} doped gehlenite ($Ca_2Al_2SiO_7$) glass-ceramics for broadband amplifier showing a broad-band emission of 1.1–1.4 μm with higher intensity than in the corresponding as-quenched glass [22]. In others works, gehlenite has been used as a host matrix for lanthanides, transition metals and rare-earth. Specifically, it has been studied by adding Ce^{3+}, Eu^{2+}, Bi^{3+}, these dopants have provided long-lasting phosphoresce and can be used as: tunable solid laser materials [23], such as single component luminophore emitting warm white light in the production of white LEDs [24], or like photoluminescence emissions in different spectral regions [25]. Recently, Ni-doped gehlenite glass microspheres have been proposed for their good magnetic properties. In this research Majerová et al., studied the magnetic behavior of the samples both for glass microspheres and crystalline samples, diamagnetic, paramagnetic and ferromagnetic components could be observed depending on whether Ni-doping is used or not, as well as depending on temperature and applied magnetic field values [17].

In general, until now the addition of second phases in gehlenite has been studied and its properties have improved, but so far have not focused on the manufacturing method or on the improvement of obtaining this transparent ceramic. SLS technique has not been yet employed to obtain semi-transparent ceramic spheres made of gehlenite, which considers short production times, economy and it is not polluting.

Therefore, in the present work, selective laser sintering technique was applied to a blend of ceramic oxide powders (SiO_2, ZnO, MgO, Na_2O, Li_2O, Al_2O_3 and CaO) to develop a semi-transparent ceramic with spherical shape, without using any additives, hence the effects of SLS on the crystalline structure, morphology, transmittance, chemical composition and thermal distribution on the sample were investigated.

Materials and methods

Selective laser sintering of powder blend

The preparation of the samples to be investigated starts with weighing all ingredients. Waste or raw materials from the ceramic industry in the northeastern Mexico region were used for all the prepared formulations. The starting materials include nepheline, spodumene, dolomite, zinc oxide, alumina and calcium oxide. All raw materials were mixed and ground in a planetary ball mill at 250 rpm for 30 min using five ZrO_2 balls with 30 mm of diameter. The powder materials obtained in this way have the following composition: (SiO_2 = 54 wt.%, Al_2O_3 = 19 wt.%, CaO = 11 wt.%, ZnO = 6 wt.%, MgO = 4 wt.%, Na_2O = 3 wt.%, K_2O = 1 wt.%, Li_2O = 1 wt.% and L.O.I = 1% wt.). Particle size measurement was carried out using a particle size analyzer from Microtrac Mod. S3500 (PA, Unites States).

Fig. 1 shows the starting powders (raw material), which have an irregular morphology, and their corresponding particle size distribution. The percentiles of the distribution are shown in Fig. 1, and the mean size of the particles of the raw material was 21.84 μm.

The ceramic oxides were chosen to develop the SACZMNKL system as follows: gehlenite is one of the most important crystalline phases in CaO–MgO–Al_2O_3–SiO_2 based glass ceramic. Gehlenite crystals have received attention due to their excellent optical and magnetic properties according to recent research [17,26]. As known, glass ceramic materials containing gehlenite crystals can be prepared using a mixture of oxides by the selective laser sintering (SLS) technique. However, given the relatively complex elemental composition, it becomes particularly important to develop a nucleating agent that can singly induce the precipitation of gehlenite crystals. MgO can be one of these nucleating agents that promotes gehlenite crystals. Additionally, the modification of CaO–MgO–Al_2O_3–SiO_2 based glass properties can occurs by adding halides or oxides of alkali, alkaline earth, and transition metals in the glass network [27]. Therefore, the structural network is altered by doping them with other elements' traces, namely alkali metals (Li+) which boost their ionic conductivity and make them useful for solid-state technology [28–34]. Furthermore, elements such as Na and K have been used to lower melting point and achieve the desired phase (gehlenite).

On the other hand, zinc oxide (ZnO) is a compound semiconductor (belonging to the IIb–VI family of compounds) with a large exciton binding energy that makes it valuable for various optoelectronic applications such as optical sensors and light emitter, solar cells, etc. [35]. Other area of great interest is the application of ZnO as a transparent conducting oxide (TCO) for solar cells. ZnO is added to the formulation to improve the optical properties of gehlenite.

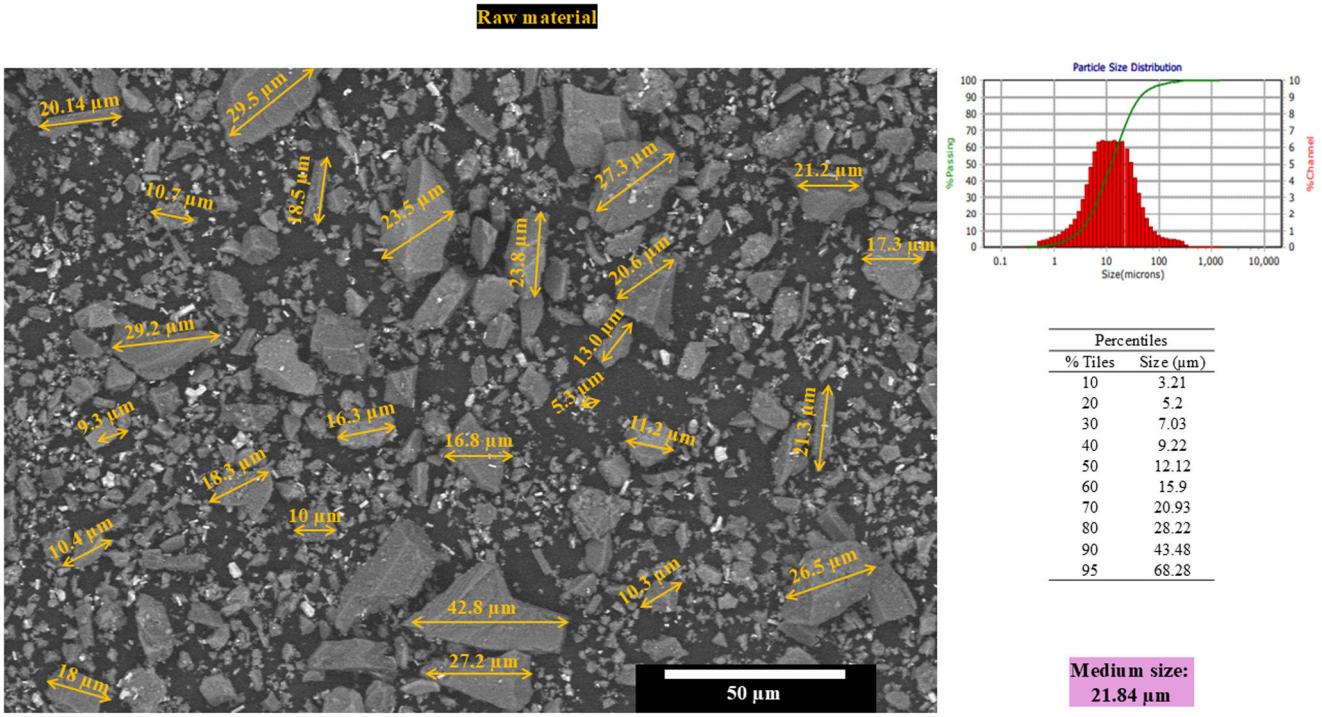

Fig. 1 – SEM micrograph of the raw material with grain size and particle size distribution.

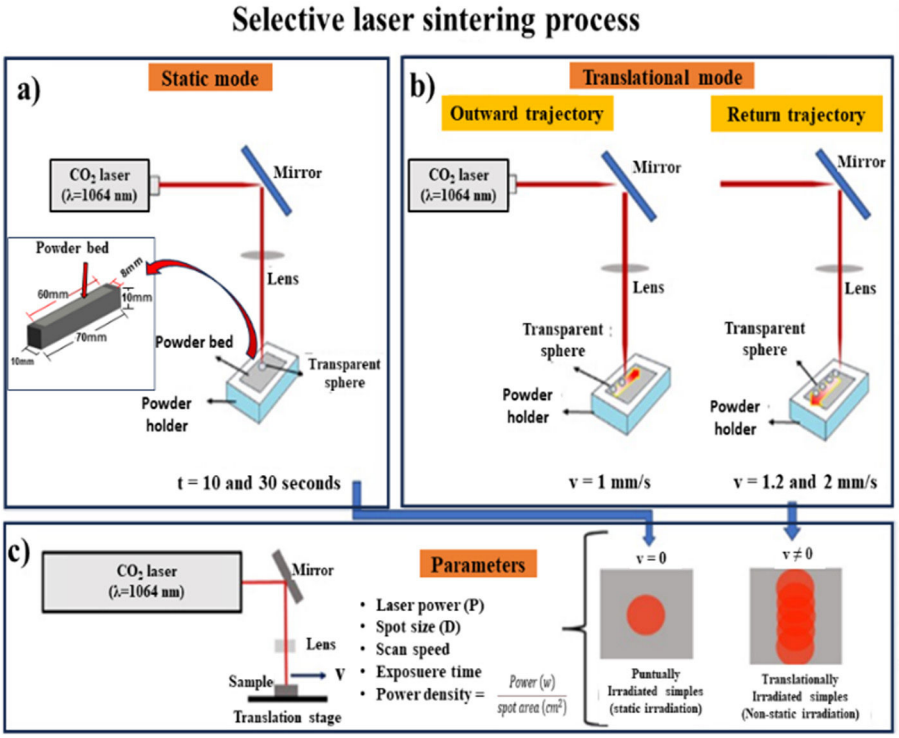

Fig. 2 – Selective laser sintering process. (a) Powder bed punctually radiated, (b) powder bed radiated by dynamic motion with 1–1.2 mm/s and 1–2 mm/s and (c) parameters used in the sintering process.

In this sense, the SACZMNKL system was studied so that every element aids in the optical properties, in lowering the melting point to crystallize the desired phase, to resist abrupt temperature changes generated after laser radiation, since these materials are considered as high temperature refractory [36].

The powder mixture was irradiated with a CO_2 laser ($\lambda = 10.6\,\mu m$) with a spot size of 100 µm, at a power of 60 W, and power density of 155 W/cm^2.

Tests were carried out in static and non-static laser radiation (dynamic mode). Fig. 2 depicts the laser sintering process carried out in this research. For the static mode, direct and

Table 1 – Experimental conditions for the different samples.

Sample	Time of radiation	Power density	Description
SI-10	10 s	155 W/cm^2	Static mode
SI-30	30 s	155 W/cm^2	Static mode
CI 1–1.2	110 s	155 W/cm^2	Dynamic mode: 1 and 1.2 mm/s
CI 1–2	90 s	155 W/cm^2	Dynamic mode: 1 and 2 mm/s

punctual laser irradiation was carried out in two different samples at 10 and 30 s, respectively (see Fig. 2(a)). For radiation on non-static radiation (dynamic mode), two scanning speed combinations were used on 60 mm long powder bed. The combinations were 1–1.2 and 1–2 mm/s (see Fig. 2(b)). With 1–1.2 mm/s, it was considered that first the laser passed through the blend of SACZMNKL at 1 mm per second and then the laser returned irradiating the same trajectory at a speed of 1.2 mm/s. With 1–2 mm/s, means that the laser advanced at 1 mm/s to return through the same area at 2 mm/s. In both radiation modes, spheres were created, due to the energy deposited by the laser in the powder bed.

Laser irradiation in both cases was performed under ambient pressure and temperature. Fig. 2(c) shows the parameters used for the radiation carried out on the powder bed. Experimental conditions of the laser irradiation of samples are summarized in Table 1.

Characterization

The crystalline structure of the samples was studied by performing XRD analysis using an Empyrean diffractometer from PANalytical (Malvern, UK). Morphology of the samples was observed through a scanning electron microscope SEM-FEI Nova 200 NanoSEM from FEI Company (Oregon, United states). Furthermore, chemical composition analysis was carried out using Raman spectroscopy. Raman spectra were collected by a Raman spectrophotometer LABram HR Evolution from Horiba (Kyoto, Japan), using a wavelength of 532 nm.

Thermal simulation

In order to evaluate the temperature distribution generated during the powder synthesis process, a simulation was carried out using the transient state finite element method using the ANSYS software (PA, United states). First, the powder bed was drawn, with dimensions of 60 mm in length, 8 mm in width and 1 mm in thickness, which was deposited on an aluminum base with dimensions of 70 mm in length, 10 mm in width and 10 mm high (see inset in Fig. 2(a)).

The density, thermal conductivity and specific heat were considered, in proportions of the oxides according to their participation percentages.

Results and discussion

Thermal analysis generated by the laser

The simulation consisted in applying a linear displacement of the energy beam on the powder bed (outward trajectory), at a constant speed of 1 mm/s, covering 60 mm. Subsequently, a second linear movement was applied in the opposite direction (return trajectory), at a speed of 1.2 mm/s.

Fig. 3(a)–(c) shows the temperature distribution at 1, 60, and 110 s respectively, that is, at the beginning and at the end of the first path (outward trajectory), and at the end of the second path (return trajectory). Fig. 3(d) shows the temperature dissipation on the powder bed after 40 s of completing the return trajectory. The behavior of the resulting temperatures, of the total route is graphically presented in Fig. 3(e).

Fig. 3(f) is the in situ temperature measurement with a thermographic camera when the laser was irradiating the powder bed. This measurement was performed to verify the analysis carried out in ANSYS. In dynamic movement, it was observed that from the first seconds, the radiation increased the temperature, and in ANSYS, 1291.6 °C was obtained at 3.3 s and 1311.2 °C was obtained with 8.8 s (see Fig. 3(e)), while with the thermographic camera it was evident that 1326.1 °C was reached at 3.52 s and 1350 °C was reached at 8.9 s (see inset in Fig. 3(f)). In both cases the temperatures obtained are close with an average variation of 37 °C.

Likewise, it was observed that in the outward trajectory, there were average temperatures of 1345 °C, and in the return trajectory the average temperatures were 1487 °C, this agrees with the thermographic photo shown in Fig. 3(e), corresponding to the return trajectory in the radiation point, which shows a temperature close to 1443 °C.

Crystalline structure

The X-ray diffraction patterns in Fig. 4 of the raw material sample (mixed mechanical powder from (SACZMNKL)) show characteristic peaks of zinc oxide (ZnO, PDF #96-230-0113), silicon oxide (SiO_2, PDF# 00-033-1161), aluminum oxide (Al_2O_3, PDF# 96-230-0449), calcium aluminium silicate ($CaAl_2(SiO)_4$, PDF #00-003-0559), calcium hydroxide ($Ca(OH)_2$, PDF# 00-044-1481) and anorthoclase ($Al_4Si_{12}Na_{2.6}K_{1.3}O_{32}$, PDF# 96-900-0857).

Due to the high energy generated within the ZrO_2 ball mill, the in situ formation of anorthite ($CaAl_2(SiO)_4$ and anorthoclase phase ($Al_4Si_{12}Na_{2.6}K_{1.3}O_{32}$) occurred, whose components match the starting powders used. Detected planes (1 −1 3) and (−2 −4 3), which diffract in 28.77° and 36.5° coincide with standard anorthite (PDF 00-003-0559). Furthermore, planes (0 2 0), (−2 2 1), (2 2 0), (1 3 1), (0 4 1), (−2 4 1), (−2 4 1), (0 6 0), and (0 6 2), which diffract in 13.63°, 25.58°, 27.45°, 30.10°, 30.84°, 35.16°, 41.74°, and 46.7°, correspond to standard anorthoclase (PDF 96-900-0857) (see Fig. 4).

The mineralogy of the sphere powders was characterized by X-ray diffraction (XRD). Fig. 5 shows the diffraction patterns of the irradiated samples with static (SI-10 and SI-30) and dynamic mode (CI 1–1.2 and CI 1–2) by SLS.

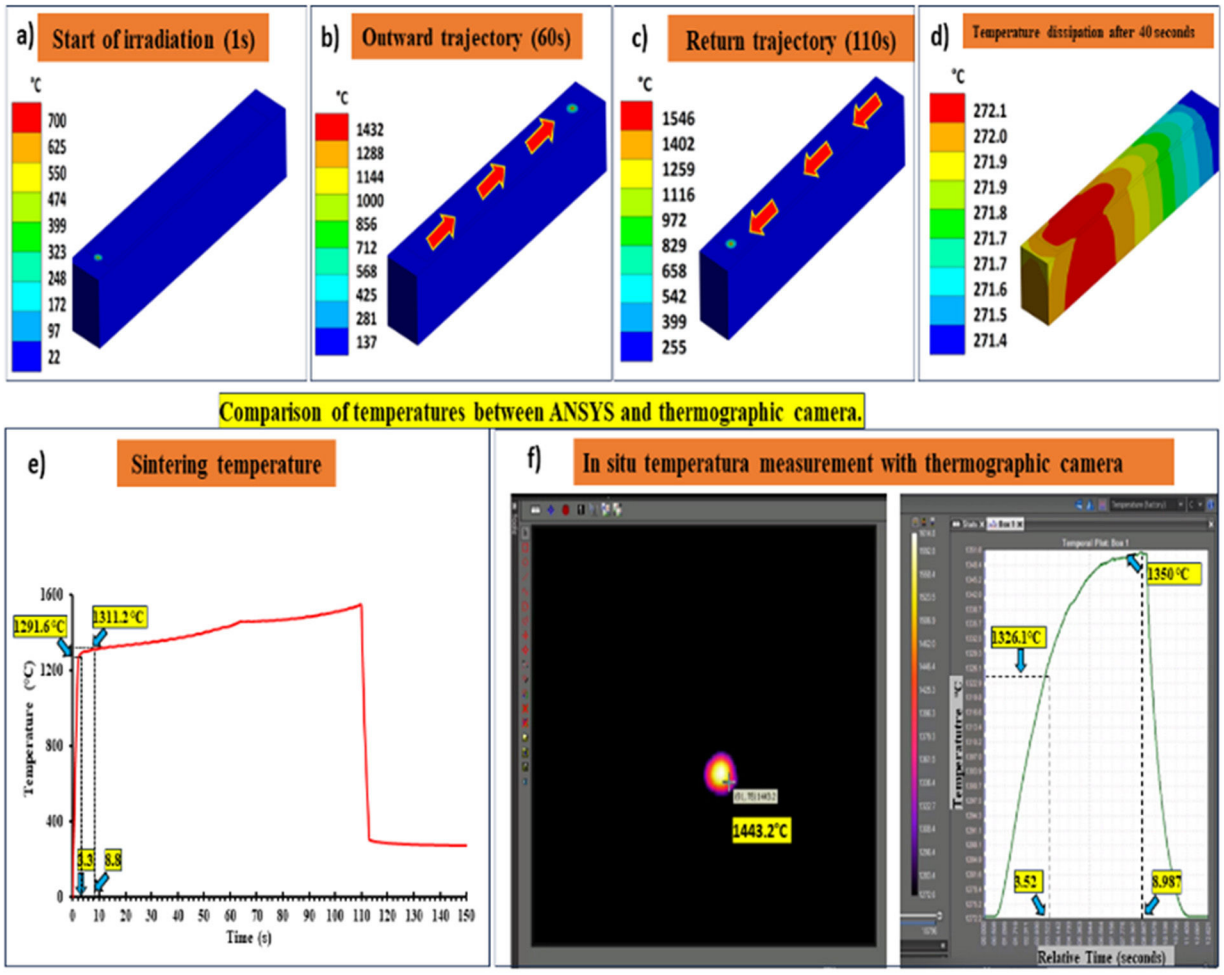

Fig. 3 – Simulation of temperatures on the powder bed using ANSYS software, irradiated in (a) 1 s, (b) 60 s, (c) 110 s, (d) temperature dissipated after 40 s, (e) temperatures reached during the radiation of both trajectories, and (f) analysis of temperatures carried out with a thermographic camera.

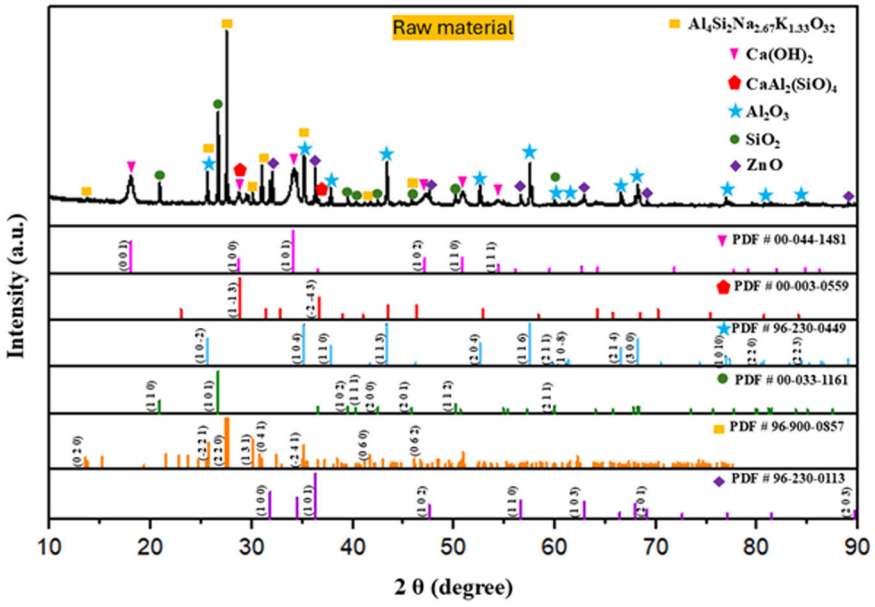

Fig. 4 – XRD analysis of the raw material.

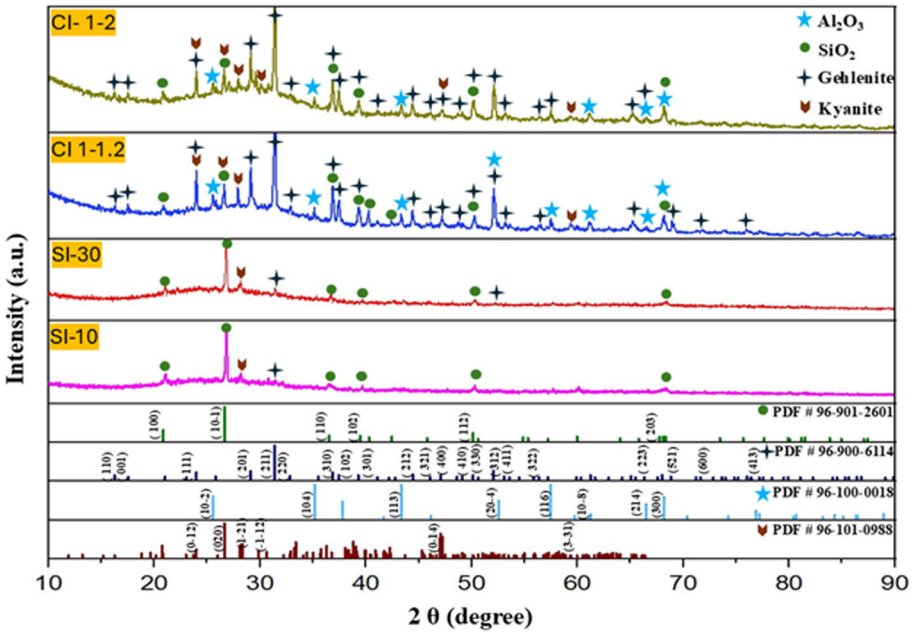

Fig. 5 – XRD analysis of the irradiated samples with static (SI-10 and SI-30) and dynamic mode (CI 1–1.2 and CI 1–2) by SLS.

The powders of the spheres obtained by radiation static (10 s and 30 s) were mineralogically analyzed. In all samples, the formation of gehlenite (1593 °C, $Ca_4Al_{4.12}Si_{1.9}O_{14}$ PDF#96-900-6114) was evident.

With 10 s, one plane (2 1 1) was detected at 31.43°. With 30 s, two peaks were evident, the formation of one more plane (3 1 2) was detected at 52.097°, corresponding to gehlenite. The kyanite phase was also detected in a lower proportion. In dynamic mode, the gehlenite phase increased with respect to the statically irradiated samples (see Fig. 5) This can be explained as follows:

1. In the first path of the beam (1 mm/s), the energy density of the laser acted for a longer time with greater energy dissipation on the powder bed (since this velocity was slower), since from 3.3 s to 60 s the temperatures found were ≈1300 °C to 1432 °C respectively, according to the simulation carried out in ANSYS, so that as the area of the beam advanced, it caused sintering temperatures to formation in situ of gehlenite between Ca, Al, Mg and Si, this agrees with Pan et al., where they comment that gehlenite can be obtained in the range of 1400–1450 °C [37].
2. On the return trajectory, a heat treatment was carried out on the spheres, with sample 1–1.2 mm/s (lower return speed) it was observed that the kyanite peaks decreased ($AlSiO_5$), attributing that with this speed a longer radiation time was obtained, causing the kyanite to transform into gehlenite. Also, in this radiation the raw material dust superficially adhered to the spheres in the first radiation path caused the in situ formation of gehlenite.

In sample 1–2 mm/s, due to the faster return velocity, higher amounts of kyanite phase were observed.

The heat dispersion had greater relevance with lower scan rates, due to the synthesis reaction for the formation of gehlenite (with 1–1.2 (lower return speed)). The results agreed with those reported by Sofia et al. [38], regarding that the most significant heat dissipation is by bed conduction and that the thermal dispersion can be reduced through an increase of the laser scanning speed.

While in the samples obtained in static radiation mode, only presented the beginning structural rearrangement for obtaining gehlenite. With this mode of radiation, only elongated semi-spheres were obtained (sometimes shapeless, see Fig. 6).

Morphology

Fig. 6 corresponds to image of the starting powders and of the studied spheres under dynamic (CI 1–2 and CI 1–1.2) and static (SI-10 and SI-30) radiation. Furthermore, using a higher magnification, the presence of the glassy phase and its distribution in the laser-irradiated spheres can be observed. The EDX analysis corresponds to the elements present in the raw material. Using a lower scanning speed (CI 1–1.2), it was observed larger diameter spheres (≈2 mm); and when a higher scanning speed was used (CI 1–2), smaller diameters (≈1.5 mm) were obtained.

Scanning electron microscopy was used to visualize the morphology of the samples. Fig. 7(a)–(d) shows the morphology of the punctually irradiated samples (SI-10 and SI-30). The punctually irradiated samples have formed a completely homogeneous surface, with no visible cracks. However, there are visible contrast areas and roughness in the surface, which is due to material that did not sintered with the glass matrix. SI-10 has more aggregates on the surface, yet their size is smaller than those on the surface of sample SI-30.

On the other hand, Fig. 7(e)–(h) corresponds to the laser-irradiated samples with dynamic mode (CI 1–1.2 and CI 1–2). Both samples show completely sintered surfaces, without cracks or contrast areas. Fig. 7(e)–(h) shows clearly that con-

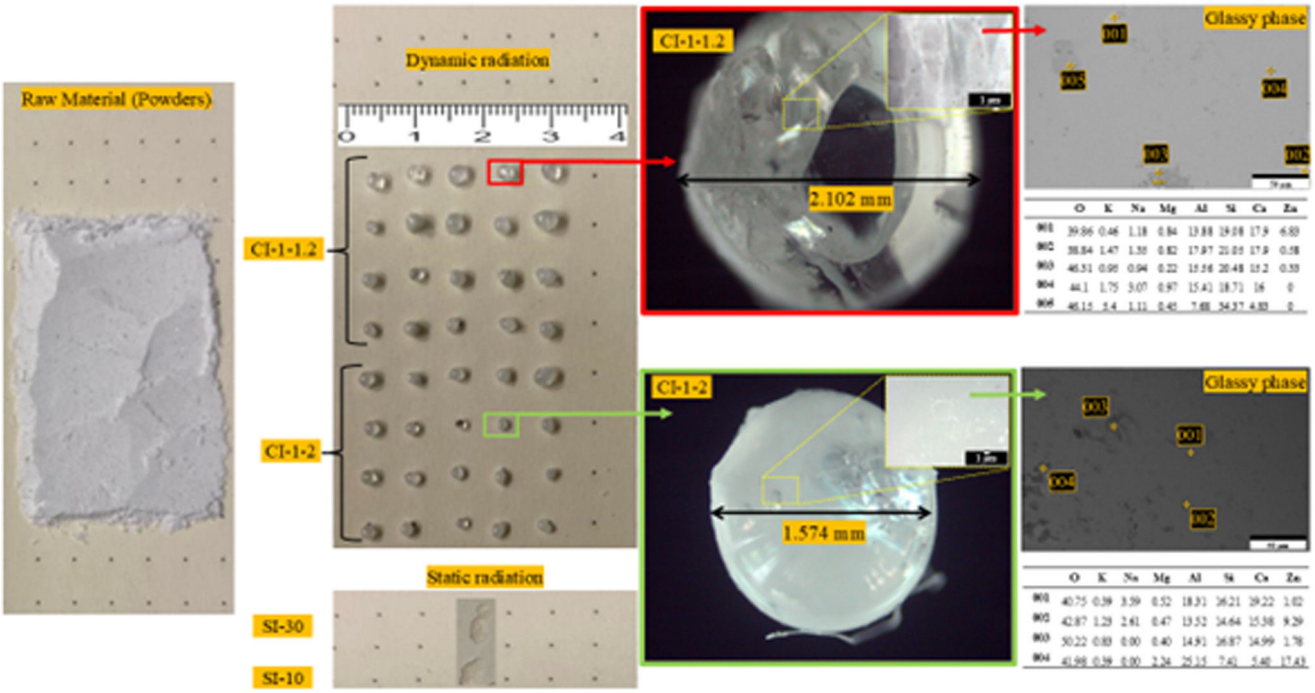

Fig. 6 – Raw material and spheres obtained under static and dynamic radiation. Glassy phase distribution in the spheres obtained under dynamic radiation.

tinuous laser radiation diminishes surface roughness on the sintered materials. Some aggregates can be seen on the sintered surfaces of CI 1–1.2 and CI 1–2, with sizes smaller than 5 μm. The greater number of aggregates on the surface of sample CI 1–2 may be due to the higher speed, which may not allow for sufficient laser–powder interaction time, thus limiting the energy transfer to completely fuse the powders into the glass matrix.

Energy-dispersive X-ray spectroscopy (EDX) was carried out to identify the elemental composition in some areas of the samples. The semiquantitative analysis of the elemental composition of the samples in wt.% is reported in the table in Fig. 7. For punctually irradiated samples, SI-10 and SI-30, the matrix exhibits the predominant presence of Si, Al and Ca. In sample SI-10, there are rod-like and spherical-like aggregates on the surface. Rod-like aggregates show a similar composition to the matrix, while EDX detected greater Ca, Mg, and Zn signals in spherical aggregates. The aggregates on sample SI-30 have crystal-like and spherical-like aggregates. Crystal-like composition resembles their matrix of the sample SI-30, with a high intensity of Si, Al and Ca signals. Conversely, spherical aggregates on sample SI-30 were mainly composed of Zn, Si, Al, and Ca.

On the other hand, samples irradiated in dynamic mode, CI 1–1.2 and CI 1–2, show similar elemental composition to the punctually irradiated samples (SI-10 and SI-30), in which Si, Al and Ca dominate the spectrum. However, the signal strength of Al and Ca appear higher in the dynamic mode, which results in a higher elemental composition percentage for these elements. This agrees with the XRD analysis (Fig. 5), where a higher percentage of the gehlenite phase was detected in dynamic mode, compared to the static mode.

Sample CI 1–1.2 exhibits spherical-like aggregates on the sintered surface. These aggregates have traces of Si, Al, and Ca. Calcium has the highest elemental composition on the aggregates, followed by silicon and aluminium. However, the elemental composition of Si varies between the aggregates, then having Si-rich and Si-poor zones. In general, it is observed that sample CI 1–1.2 obtained homogeneous surfaces with completely sintered areas and a lower concentration of aggregates.

Sample CI 1–2 shows flake-like and spherical-like aggregates. EDS has detected traces of Si, Ca, Al, and Zn in flake-like aggregates, while spherical aggregates are composed of Ca, Si and Al. In both types of aggregates, calcium has the greatest elemental composition, followed by Si, Al and Zn.

Raman spectroscopy

Raman spectra of the punctually and dynamically irradiated materials are exhibited in Fig. 8(a). Sample SI-10 does not show many changes with respect to the raw material. The spectrum recorded for this sample consisted mainly of broad bands with low intensity, which means that the ceramic material resembles a glassy system, and that the laser exposure time may not be sufficient to induce crystallization of the system. On the other hand, Sample SI-30 shows broad peaks in the high frequency region, centered at 828, 950, 1073 and 1171 cm^{-1}. The appearance of these broad bands shows that the laser sintering procedure has the capability of working near the glass transition temperature, where the broad bands in the region 1000–1200 cm^{-1} increase in intensity and width forming a unique band [39]. Peaks in this region are associated to the vibrations of the

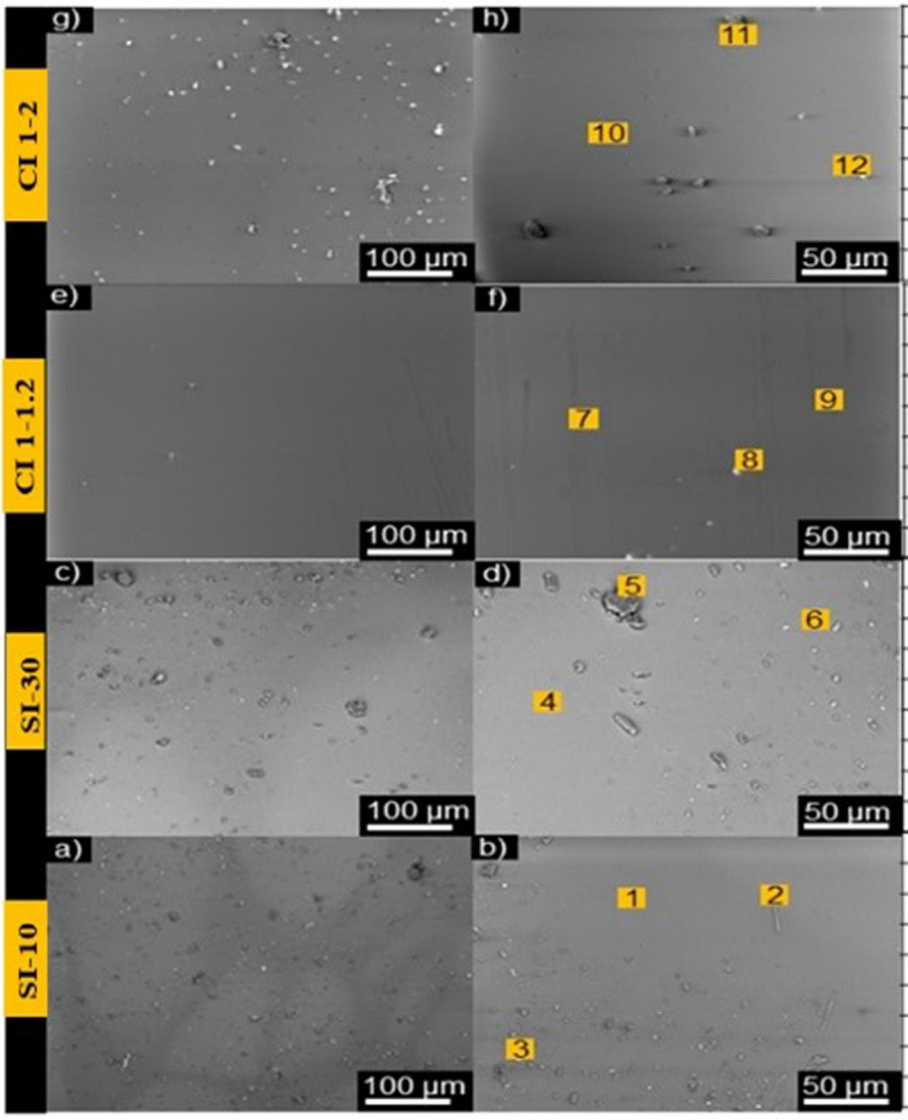

wt.%)

Element	10	11	12
K	2.05	1.23	0.00
O	54.65	49.32	61.37
Na	3.91	0.00	0.70
Mg	0.16	0.00	0.00
Al	12.02	7.07	1.76
Si	14.00	8.91	2.42
Ca	13.19	27.59	33.75
Zn	0.00	5.89	0.00
Element	**7**	**8**	**9**
K	1.77	0.84	1.95
O	41.04	56.16	38.49
Na	1.84	1.18	0.00
Mg	0.42	0.45	0.40
Al	11.75	6.30	12.53
Si	21.58	9.99	22.15
Ca	21.60	25.08	21.17
Zn	0.00	0.00	3.31
Element	**4**	**5**	**6**
K	1.66	0.00	0.92
O	52.37	49.22	39.70
Na	1.20	6.19	0.00
Mg	1.18	2.11	0.00
Al	7.55	8.04	5.92
Si	26.18	25.36	17.79
Ca	5.57	9.08	4.37
Zn	4.30	0.00	31.30
Element	**1**	**2**	**3**
K	2.03	2.73	1.77
O	51.56	49.86	50.54
Na	3.15	2.89	1.35
Mg	0.92	1.05	2.73
Al	6.52	6.89	4.80
Si	31.58	31.99	21.68
Ca	4.23	4.60	13.09
Zn	0.00	0.00	4.06

Fig. 7 – SEM micrographs of irradiated samples, (a and b) punctually with 10 s, (c and d) punctually with 30 s, (e and f) irradiated with a speed of 1–1.2 mm/s, and (g and h) samples irradiated with a speed of 1–2 mm/s. On the right of the figure is EDX point semiquantitative analysis performed on different parts of the irradiated samples.

Si–O and Si–O–Si linkages, with structural units $Q^0([SiO_4]^{4-}$ at 850 cm^{-1}), $Q^1([Si_2O_7]^{6-}$ at 880 cm^{-1}), $Q^2([SiO_3]^{2-}$ between 950 and 1000 cm^{-1}), $Q^3([Si_2O_4]^{2-}$ at 1050 cm^{-1}) and $Q^4([SiO_2]$ at 1150 cm^{-1}) [40]. The peaks are slightly redshifted due to the presence of high amounts of Al_2O_3 in the powder mixture [41]. The main structural units acting on the sample are Q^3 and Q^2, thus the glass matrix is polymerized in chains and sheets [42]. The broad peak centered at 828 cm^{-1} could be associated to the symmetric Si–O–Al stretching (830–850 cm^{-1}), the symmetric $Al–O^-$ stretching (790–800 cm^{-1}) and the Q^0 structural unit (850–880 cm^{-1}) [39]. This peak appears from the laser sintering process, since it does not appear on the Raman spectrum for the raw material and confirms the incorporation of tetrahedral $[AlO_4]^{5-}$ units into the glass matrix, which act as network formers [43]. The sharp peak at 710 cm^{-1} could be associated with the Si–O–Si symmetric stretching [44]. The band near 545 cm^{-1} with the band near 589 cm^{-1} could be indicatives of sodium-containing silicates, these bands form a single band in Al_2O_3-free mixtures. This separation is due to the presence of Al–O–Al bridges [45–47]. Furthermore, the presence of alkali metal and alkali earth cations, such as Li^{1+}, Na^{1+}, Mg^{2+} and Ca^{2+}, is confirmed with the peaks in the range 200–500 cm^{-1}, which are assigned to the broken $Si–O^-$ bonds that are typical of their action as network modifiers, and to the increment of the intensity in the peak 1073 cm^{-1} [48] and the broadness of the band at 950 cm^{-1}, which is due to the stabilization of the glassy network though charge compensation of the Al structural units [39].

Raman spectra of samples irradiated in dynamic mode (CI 1–1.2 and CI 1–2) are shown in Fig. 8(b). These spectra show that the material has been crystallized during the laser sintering process, since we obtain higher intensities than in the

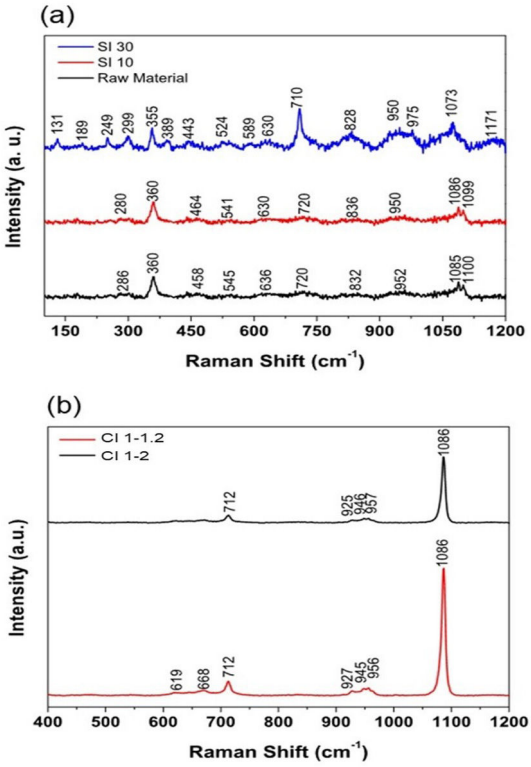

Fig. 8 – (a) Raman spectra for statically irradiated samples. (b) Raman spectra for samples irradiated in dynamic mode.

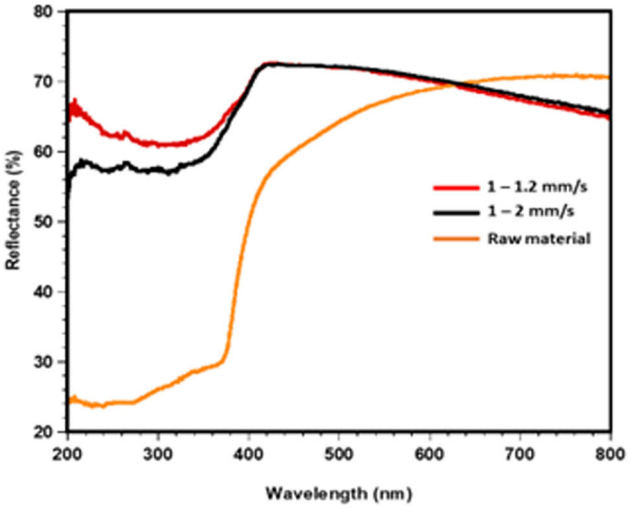

Fig. 9 – UV–vis spectra of powders and irradiated samples by dynamic mode at 1–1.2 and 1–2 mm/s.

punctually irradiated samples and greater signal-to-noise ratio. In the high frequency region, 800–1200 cm^{-1}, there are some peaks at 927, 947, 956, and 1086 cm^{-1}. The peak centered at 927 cm^{-1} is related to the vibration Q^1 structural unit, while peaks in the range of 956–1000 cm^{-1} are assigned to the vibrations of Q^2 structural units. The peak at 1086 cm^{-1} is associated with the vibration of Q^3 structural unit, which is the most prominent peak and thus the matrix is polymerized mainly in a sheet form. Peaks between 600 and 800 cm^{-1} are associated to the vibrations of T–O–T bridges (T = Si, Al) [49]. It is not possible to find out the incorporation of the other ceramic oxides into the glassy network due to the high intensities of the peaks associated with silica and alumina. One possible explanation for this is that during the laser sintering process, the laser power density was sufficient to melt SiO_2 completely, incorporate Al^{3+} cations into the network and encapsulate the other ceramic powders inside the manufactured ceramic part.

Optical properties

The optical properties of three significant samples: powders mix (SACZMNKL) and samples irradiated by dynamic mode (1–1.2 and 1–2 mm/s) were analyzed using UV–visible spectroscopy, the results of which are shown in Fig. 9.

Fig. 9 shows that the UV zone (200–380 nm) had the lowest reflectance values across the board for all studied instances. In the case of powders, reflectance values began to increase from 380 nm, and in the visible spectrum zone (400 and 800 nm) the highest value was 70% reflectance at 700 nm. In the case of samples in dynamic mode values varied from 52 to 66% R and 64 to 67% R for 1–2 and 1–1.2 mm/s, in the SEM analysis these specimens show a more homogeneous morphology compared to the samples with static radiation.

Likewise, it can be observed that in the visible zone an opposite trend occurred between the raw material and the samples in dynamic mode, while the raw materials increased their R, both samples in dynamic mode decreased their R. In the visible zone visible, specifically from 640 nm to 800 nm for sample 1–1.2, the lowest reflectance was obtained, which varied from 70 to 64%.

In general, semi-transparent characteristics were obtained for the samples irradiated in dynamic mode because the synthesis of the spheres caused by laser energy favors the growth of gehlenite crystals. Other ceramic glasses with crystalline and amorphous phases present a behavior comparable to this one [50,51].

Conclusions

Selective laser sintering was applied to the SACZMNKL oxide mixture using a CO_2 laser (10.6 μm), both static and dynamic mode. XRD shows the induction of crystalline phases of interest, such as gehlenite and kyanite, via laser irradiation. Punctually irradiated samples show aggregates on the surface, suggesting that laser interaction time with the mixture was not sufficient to bind every component into the silica matrix, whereas dynamic laser irradiation has sufficient energy to form a homogenous surface with no cracks and fewer aggregates. Raman spectra confirmed the polymerization of the silica matrix and the incorporation of aluminium atoms into the network. The mechanism of the laser sintering process of the mixture (SACZMNKL) was carried out by the addition of the ceramic oxides into a silica matrix, through the sintering process of SiO_2 due to sufficient laser irradiation. Moreover, the thermal properties of the laser sintered ceramic samples show that the material has thermal stability, and that selective laser sintering achieves the

crystallization of the phases of interest, when adequate exposure times are selected. Non-static radiation (dynamic mode) has shown overall better results, in comparison with punctually irradiated samples. Optimum properties were obtained with laser irradiation conditions of sample CI 1–1.2 mm/s.

Competing interest

The authors declare no conflict of interests.

Acknowledgements

Linda Viviana García-Quiñonez acknowledges the grant (Ciencia Básica y de Frontera 2023-2024 program) CBF2023-2024-657 by CONAHCYT-México. Cristian Córdova Mayo appreciates the support provided by the SIREI project (Universidad Veracruzana).

Alan Castillo-Rodríguez acknowledges the grant (Ciencia Básica y de Frontera program) CF-2023-I-719 by CONAHCYT-México.

REFERENCES

[1] S. Kumar, Selective laser sintering: a qualitative and objective approach, JOM 55 (10) (2003) 43–47, http://dx.doi.org/10.1007/s11837-003-0175-y.
[2] B.C. Gross, J.L. Erkal, S.Y. Lockwood, C. Chen, D.M. Spence, Evaluation of 3D printing and its potential impact on biotechnology and the chemical sciences, Anal. Chem. 86 (7) (2014) 3240–3253, http://dx.doi.org/10.1021/ac403397r.
[3] T. Chen, Y. Zhang, Thermal modeling of laser sintering of two-component metal powder on top of sintered layers via multi-line scanning, Appl. Phys. A 86 (2) (2007) 213–220, http://dx.doi.org/10.1007/s00339-006-3739-1.
[4] P. Bertrand, F. Bayle, C. Combe, P. Goeuriot, I. Smurov, Ceramic components manufacturing by selective laser sintering, Appl. Surf. Sci. 254 (4) (2007) 989–992, http://dx.doi.org/10.1016/j.apsusc.2007.08.085.
[5] Y. Li, Y. Hu, W. Cong, L. Zhi, Z. Guo, Additive manufacturing of alumina using laser engineered net shaping: effects of deposition variables, Ceram. Int. 43 (10) (2017) 7768–7775, http://dx.doi.org/10.1016/j.ceramint.2017.03.085.
[6] K. Shahzad, J. Deckers, S. Boury, B. Neirinck, J.-P. Kruth, J. Vleugels, Preparation and indirect selective laser sintering of alumina/PA microspheres, Ceram. Int. 38 (2) (2012) 1241–1247, http://dx.doi.org/10.1016/j.ceramint.2011.08.055.
[7] Z. Chen, et al., 3D printing of ceramics: a review, J. Eur. Ceram. Soc. 39 (4) (2019) 661–687, http://dx.doi.org/10.1016/j.jeurceramsoc.2018.11.013.
[8] Y. Yamauchi, T. Kigure, K. Isoda, T. Niino, Powder bed penetration depth control in laser sintering and effect on depth of fusion, Addit. Manuf. 46 (2021) 102219, http://dx.doi.org/10.1016/j.addma.2021.102219.
[9] A.B. Peters, et al., Selective laser sintering in reactive atmospheres: towards in-situ synthesis of net-shaped carbide and nitride ceramics, Addit. Manuf. 45 (2021) 102052, http://dx.doi.org/10.1016/j.addma.2021.102052.
[10] H. Wang, et al., 3D printing of transparent spinel ceramics with transmittance approaching the theoretical limit, Adv. Mater. 33 (15) (2021) 2007072, http://dx.doi.org/10.1002/adma.202007072.
[11] J. Petit, et al., Sintering of α-alumina for highly transparent ceramic applications, J. Eur. Ceram. Soc. 31 (11) (2011) 1957–1963, http://dx.doi.org/10.1016/j.jeurceramsoc.2011.04.034.
[12] Y. Sun, S. Shimai, X. Peng, G. Zhou, H. Kamiya, S. Wang, Fabrication of transparent Y_2O_3 ceramics via aqueous gelcasting, Ceram. Int. 40 (6) (2014) 8841–8845, http://dx.doi.org/10.1016/j.ceramint.2014.01.106.
[13] S.F. Wang, et al., Transparent ceramics: processing, materials and applications, Prog. Solid State Chem. 41 (1) (2013) 20–54, http://dx.doi.org/10.1016/j.progsolidstchem.2012.12.002.
[14] Y. Fang, R. Roy, D.K. Agrawal, D.M. Roy, Transparent mullite ceramics from diphasic aerogels by microwave and conventional processings, Mater. Lett. 28 (1) (1996) 11–15, http://dx.doi.org/10.1016/0167-577X(96)00028-6.
[15] S. Cohen, B. Ratzker, S. Kalabukhov, N. Frage, Diffusion bonding of transparent ceramics by spark plasma sintering (SPS) complemented by hot isostatic pressing (HIP), J. Eur. Ceram. Soc. 43 (14) (2023) 6628–6633, http://dx.doi.org/10.1016/j.jeurceramsoc.2023.06.071.
[16] B. Ratzker, A. Wagner, S. Kalabukhov, N. Frage, Transparent Er_2O_3 ceramics fabricated by high-pressure spark plasma sintering, J. Eur. Ceram. Soc. 40 (13) (2020) 4700–4703, http://dx.doi.org/10.1016/j.jeurceramsoc.2020.05.056.
[17] M. Majerová, et al., Structure and magnetic properties of Ni-doped gehlenite glass microspheres, J. Magn. Magn. Mater. 546 (2022) 168859, http://dx.doi.org/10.1016/j.jmmm.2021.168859.
[18] G.C. Wei, W.H. Rhodes, Sintering of translucent alumina in a nitrogen–hydrogen gas atmosphere, J. Am. Ceram. Soc. 83 (7) (2000) 1641–1648, http://dx.doi.org/10.1111/j.1151-2916.2000.tb01443.x.
[19] F.W. Vahldiek, Translucent ZrO_2 prepared at high pressures, J. Less Common Met. 13 (5) (1967) 530–540, http://dx.doi.org/10.1016/0022-5088(67)90087-2.
[20] L. Jin, G. Zhou, S. Shunzo, J. Zhang, S. Wang, ZrO_2-doped Y_2O_3 transparent ceramics via slip casting and vacuum sintering, J. Eur. Ceram. Soc. 30 (2010) 2139–2143, http://dx.doi.org/10.1016/j.jeurceramsoc.2010.04.004.
[21] Q. Chen, Y. Shi, L. An, J. Chen, J. Shi, Fabrication and photoluminescence characteristics of Eu^{3+}-doped Lu_2O_3 transparent ceramics, J. Am. Ceram. Soc. 89 (2006) 2038–2042, http://dx.doi.org/10.1111/j.1551-2916.2006.01016.x.
[22] H. Yamazaki, S. Tanabe, Transparent Cr^{4+}-doped gehlenite ($Ca_2Al_2SiO_7$) glass-ceramics for broadband amplifier, in: Optical Amplifiers and Their Applications, OSA Technical Digest Series, Paper WC1, Optica Publishing Group, Otaru, 2003, http://dx.doi.org/10.1364/OAA.2003.WC1, Available from: https://opg.optica.org/abstract.cfm?URI=OAA-2003-WC1.
[23] N. Kodama, Y. Tanii, M. Yamaga, Optical properties of long-lasting phosphorescent crystals Ce^{3+}-doped $Ca_2Al_2SiO_7$ and $CaYAl_3O_7$, J. Lumin. 87–89 (2000) 1076–1078, http://dx.doi.org/10.1016/S0022-2313(99)00543-8.
[24] P. Yang, X. Yu, H. Yu, T. Jiang, D. Zhou, J. Qiu, Effects of crystal field on photoluminescence properties of $Ca_2Al_2SiO_7$:Eu^{2+} phosphors, J. Rare Earths 30 (12) (2012) 1208–1212, http://dx.doi.org/10.1016/S1002-0721(12)60207-5.
[25] M. Majerová, R. Klement, A. Prnová, J. Kraxner, E. Bruneel, D. Galusek, Crystallization and visible-near-infrared luminescence of Bi-doped gehlenite glass, R. Soc. Open Sci. 5 (12) (2018) 181667, http://dx.doi.org/10.1098/rsos.181667.
[26] Y. Shi, X.-X. Han, R.-X. Yang, B.-Y. Chai, Y.-Y. Sun, S.-K. Li, Epitaxial growth of gehlenite in CaO–MgO–Al_2O_3–SiO_2 based glass ceramic induced by Nb_2O_5 addition, Ceram. Int. 50 (16) (2024) 28266–28274, http://dx.doi.org/10.1016/j.ceramint.2024.05.126.

[27] C. Mugoni, M. Montorsi, C. Siligardi, H. Jain, Electrical conductivity of copper lithium phosphate glasses, J. Non-cryst. Solids 383 (2014) 137–140, http://dx.doi.org/10.1016/j.jnoncrysol.2013.04.048.
[28] S. Rani, S. Sanghi, N. Ahlawat, A. Agarwal, Crystallization kinetics, optical and dielectric properties of Li_2O–CdO–Bi_2O_3–SiO_2 glasses, J. Mol. Struct. 1098 (2015) 1–11, http://dx.doi.org/10.1016/j.molstruc.2015.05.017.
[29] M.S. Shams, Y.S. Rammah, F.I. El-Agawany, R.A. Elsad, Synthesis, structure, physical, dielectric characteristics, and gamma-ray shielding competences of novel P_2O_5–Li_2O–ZnO–CdO glasses, J. Mater. Sci.: Mater. Electron. 32 (2) (2021) 1877–1887, http://dx.doi.org/10.1007/s10854-020-04956-6.
[30] M.S. Sutrisno, N.M. Samsudin, E.S. Sazali, R. Hisam, AC conductivity and dielectric properties of $98[20Li_2O–xBi_2O_3–(80-x)TeO_2]$–2Ag mixed ionic–electronic glasses, J. Mater. Sci.: Mater. Electron. 32 (4) (2021) 5138–5155, http://dx.doi.org/10.1007/s10854-021-05246-5.
[31] T. Liang, J. Zhang, H. Chen, L. Gao, S. Qu, V.G. Harris, Impact of alkaline earth oxides on dielectric properties of photoetchable glasses as interposers for integrated circuits packaging, J. Alloys Compd. 874 (2021) 159546, http://dx.doi.org/10.1016/j.jallcom.2021.159546.
[32] M. Boora, et al., Investigation of structural and impedance spectroscopic properties of borate glasses with high Li^+ concentration, Solid State Ionics 368 (2021) 115704, http://dx.doi.org/10.1016/j.ssi.2021.115704.
[33] M. Monisha, et al., Structural, dielectric, optical and photoluminescence studies of Tm^{3+} doped B_2O_3–BaO–MgO–Li_2O–Na_2O–LiF glasses featuring strong blue emission, J. Non-cryst. Solids 560 (2021) 120733, http://dx.doi.org/10.1016/j.jnoncrysol.2021.120733.
[34] H.H. Somaily, H. Algarni, Y.S. Rammah, A. Alalawi, C. Mutuwong, M.S. Al-Buriahi, The effects of V_2O_5/K_2O substitution on linear and nonlinear optical properties and the gamma ray shielding performance of TVK glasses, Ceram. Int. 47 (1) (2021) 1012–1020, http://dx.doi.org/10.1016/j.ceramint.2020.08.215.
[35] K.J. Chen, et al., The crystallization and physical properties of Al-doped ZnO nanoparticles, Appl. Surf. Sci. 254 (18) (2008) 5791–5795, http://dx.doi.org/10.1016/j.apsusc.2008.03.080.
[36] L.F. Verdeja, E. Sintesis, Refractory and Ceramic Materials, Editorial Síntesis, Spain, 2008.
[37] X. Pan, D. Zhang, Y. Wu, H. Yu, Synthesis and characterization of calcium aluminate compounds from gehlenite by high-temperature solid-state reaction, Ceram. Int. 44 (12) (2018) 13544–13550, http://dx.doi.org/10.1016/j.ceramint.2018.04.186.
[38] D. Sofia, M. Granese, D. Barletta, M. Poletto, Laser sintering of unimodal distributed glass powders of different size, Proc. Eng. 102 (2015) 749–758, http://dx.doi.org/10.1016/j.proeng.2015.01.180.
[39] E. Gao, W. Wang, L. Zhang, Effect of alkaline earth metal oxides on the viscosity and structure of the CaO–Al_2O_3 based mold flux for casting high-al steels, J. Non-cryst. Solids 473 (2017) 79–86, http://dx.doi.org/10.1016/j.jnoncrysol.2017.07.029.
[40] K. Pasiut, J. Partyka, M. Lesniak, P. Jelen, Z. Olejniczak, Raw glass-ceramics glazes from SiO_2–Al_2O_3–CaO–MgO–Na_2O–K_2O system modified by ZrO_2 addition – changes of structure, microstructure and surface properties, Open Ceram. 8 (2021) 100188, http://dx.doi.org/10.1016/j.oceram.2021.100188.
[41] J. Cheng, Z. Xiao, K. Yang, H. Wu, Viscosity, fragility and structure of Na_2O–CaO–Al_2O_3–SiO_2 glasses of increasing Al/Si ratio, Ceram. Int. 39 (4) (2013) 4055–4062, http://dx.doi.org/10.1016/j.ceramint.2012.10.258.
[42] K. Zheng, J. Liao, X. Wang, Z. Zhang, Raman spectroscopic study of the structural properties of CaO–MgO–SiO_2–TiO_2 slags, J. Non-cryst. Solids 376 (2013) 209–215, http://dx.doi.org/10.1016/j.jnoncrysol.2013.06.003.
[43] K. Ariane, A. Tamayo, A. Chorfa, F. Rubio, J. Rubio, Effect of P_2O_5 and Al_2O_3 on crystallization, structure, microstructure and properties of Li_2O–MgO–Al_2O_3–SiO_2–TiO_2–ZrO_2 glass ceramics, Bol. Soc. Esp. Cerám. V. 61 (2020), http://dx.doi.org/10.1016/j.bsecv.2020.08.004.
[44] Y. Shi, X.-X. Han, B.-W. Li, Y.-X. Chen, M.-X. Zhang, Modification of glass network and crystallization of CaO–Al_2O_3–MgO–SiO_2 based glass ceramics with addition of iron oxide, Ceram. Int. 46 (7) (2020) 9207–9217, http://dx.doi.org/10.1016/j.ceramint.2019.12.173.
[45] T.K. Bechgaard, G. Scannell, L. Huang, R.E. Youngman, J.C. Mauro, M.M. Smedskjaer, Structure of MgO/CaO sodium aluminosilicate glasses: Raman spectroscopy study, J. Non-cryst. Solids 470 (2017) 145–151, http://dx.doi.org/10.1016/j.jnoncrysol.2017.05.014.
[46] S. Kucharczyk, M. Sitarz, M. Zajac, J. Deja, The effect of CaO/SiO_2 molar ratio of CaO–Al_2O_3–SiO_2 glasses on their structure and reactivity in alkali activated system, Spectrochim. Acta Part A: Mol. Biomol. Spectrosc. 194 (2018) 163–171, http://dx.doi.org/10.1016/j.saa.2018.01.018.
[47] M. Gajek, M. Leśniak, M. Sitarz, E. Stodolak-Zych, A. Rapacz-Kmita, The crystallization and structure features of glass within the K_2O–MgO–CaO–Al_2O_3–SiO_2–(BaO) system, J. Mol. Struct. 1220 (2020) 128747, http://dx.doi.org/10.1016/j.molstruc.2020.128747.
[48] F. Pei, et al., Influence of low magnesia content on the CaO–Al_2O_3–SiO_2 glass-ceramics: its crystallization behaviour, microstructure and physical properties, Ceram. Int. 44 (16) (2018) 20132–20139, http://dx.doi.org/10.1016/j.ceramint.2018.07.306.
[49] F. Pei, G. Zhu, P. Li, H. Guo, P. Yang, Effects of CaF_2 on the sintering and crystallisation of CaO–MgO–Al_2O_3–SiO_2 glass-ceramics, Ceram. Int. 46 (11) (2020) 17825–17835, http://dx.doi.org/10.1016/j.ceramint.2020.04.089 [Part A].
[50] W. Tang, et al., CoO-doped MgO–Al_2O_3–SiO_2-colored transparent glass-ceramics with high crystallinity, Appl. Phys. A 24 (2) (2018) 191, http://dx.doi.org/10.1007/s00339-017-1537-6.
[51] E. Bernardo, L. Fiocco, A. Prnová, R. Klement, D. Galusek, Gehlenite:Eu^{3+} phosphors from a silicone resin and nano-sized fillers, Opt. Mater. 36 (7) (2014) 1243–1249, http://dx.doi.org/10.1016/j.optmat.2014.03.007.